Draft version May 19, 2010
Preprint typeset using LaTeX style emulateapj v. 11/10/09

arXiv:1005.3027v1 [astro-ph.EP] 17 May 2010

NEAR-INFRARED THERMAL EMISSION FROM THE HOT JUPITER TRES-2B: GROUND-BASED DETECTION OF THE SECONDARY ECLIPSE*

Bryce Croll[1], Loic Albert[2], David Lafreniere[3], Ray Jayawardhana[1], Jonathan J. Fortney[4]

Draft version May 19, 2010

ABSTRACT

We present near-infrared Ks-band photometry bracketing the secondary eclipse of the hot Jupiter TrES-2b using the Wide-field Infrared Camera on the Canada-France-Hawaii Telescope. We detect its thermal emission with an eclipse depth of $0.062^{+0.013}_{-0.011}\%$ (5σ). Our best-fit secondary eclipse is consistent with a circular orbit (a 3σ upper limit on the eccentricity, e, and argument or periastron, ω, of $|e\cos\omega| < 0.0090$), in agreement with mid-infrared detections of the secondary eclipse of this planet. A secondary eclipse of this depth corresponds to a day-side Ks-band brightness temperature of $T_B = 1636^{+79}_{-88}$ K. Our thermal emission measurement when combined with the thermal emission measurements using Spitzer/IRAC from O'Donovan and collaborators suggest that this planet exhibits relatively efficient day to night-side redistribution of heat and a near isothermal dayside atmospheric temperature structure, with a spectrum that is well approximated by a blackbody. It is unclear if the atmosphere of TrES-2b requires a temperature inversion; if it does it is likely due to chemical species other than TiO/VO as the atmosphere of TrES-2b is too cool to allow TiO/VO to remain in gaseous form. Our secondary eclipse has the smallest depth of any detected from the ground at around 2 μm to date.

Subject headings: planetary system – stars: individual: TrES-2 – techniques: photometric – eclipses – infrared: planetary systems

1. INTRODUCTION

The first detection of the transit of an exoplanet in front of its parent star (Charbonneau et al. 2000; Henry et al. 2000) opened a new avenue to determine the characteristics of these exotic worlds. For all but the most eccentric cases, approximately half-an-orbit after their transits these planets pass behind their star along our line of sight allowing their thermal flux to be measured in the infrared. The first detections of an exoplanet's thermal emission (Charbonneau et al. 2005; Deming et al. 2005) came from observations in space with Spitzer using the Infrared Array Camera (IRAC; Fazio et al. 2004). Since then the vast majority of such measurements have been made using Spitzer at wavelengths longer than 3 μm, and thus longwards of the blackbody peak of these "hot" exoplanets. Recent observations have extended secondary eclipse detections into the near-infrared; the first detection was from space with NICMOS on the Hubble Space Telescope (Swain et al. 2009 at $\sim$2 μm). More recently, near-infrared detections have been achieved from the ground; the first of these detections include a $\sim 6\sigma$ detection in K-band of TrES-3b using the William Herschel Telescope (de Mooij & Snellen 2009), a $\sim 4\sigma$ detection in z'-band of OGLE-TR-56b using Magellan and the Very Large Telescope (VLT; Sing & Lopez-Morales 2009), and a $\sim 5\sigma$ detection at $\sim$2.1 μm of CoRoT-1b also with the VLT (Gillon et al. 2009).

Thermal emission measurements in the near-infrared are crucial to our understanding of these planets' atmospheres, as they allow us to constrain hot Jupiters' thermal emission near their blackbody peaks. The combination of Spitzer/IRAC and near-infrared thermal emission measurements allows us to constrain the temperature-pressure profiles of these planets' atmospheres over a range of pressures (Fortney et al. 2008), better estimate the bolometric luminosity of these planets' dayside emission, and thus contributes to a more complete understanding of how these planets transport heat from the day to nightside at a variety of depths and pressures in their atmospheres (Barman 2008).

The transiting hot Jupiter TrES-2b orbits a G0 V star with a period of $\sim$2.47 d (O'Donovan et al. 2006). According to the Fortney et al. (2008) theory this places TrES-2b marginally in the hottest, mostly highly irradiated class (the pM-class) of hot Jupiters and close to the dividing line between this hottest class and the merely warm class of hot Jupiters (the pL-class). Thus TrES-2b could be a key object to refine the dividing line between these two classes, and indicate the physical cause of this demarcation, or reveal whether this divide even exists. Recently O'Donovan et al. (2009) used Spitzer/IRAC to measure the depth of the secondary eclipse of TrES-2b in the four IRAC bands. Their best-fit eclipses are consistent with a circular orbit, and collectively they are able to place a 3σ limit on the eccentricity, e, and argument of periastron, ω, of $|e\cos\omega|$

[1] Deptartment of Astronomy and Astrophysics, University of Toronto, 50 St. George Street, Toronto, ON M5S 3H4, Canada; croll@astro.utoronto.ca
[2] Canada-France-Hawaii Telescope Corporation, 65-1238 Mamalahoa Highway, Kamuela, HI 96743.
[3] Département de physique, Université de Montréal, C.P. 6128 Succ. Centre-Ville, Montréal, QC, H3C 3J7, Canada
[4] Department of Astronomy and Astrophysics, University of California, Santa Cruz, CA, 95064

* Based on observations obtained with WIRCam, a joint project of CFHT, Taiwan, Korea, Canada, France, at the Canada-France-Hawaii Telescope (CFHT) which is operated by the National Research Council (NRC) of Canada, the Institute National des Sciences de l'Univers of the Centre National de la Recherche Scientifique of France, and the University of Hawaii.

< 0.0036. Their best-fit eclipses at 3.6, 5.8 and 8.0 μm are well-fit by a blackbody. At 4.5 μm they detect excess emission, in agreement with the theory of several researchers (Fortney et al. 2008; Burrows et al. 2008) that predicts such excess due to water emission, rather than absorption, at this wavelength due to a temperature inversion in the atmosphere. One-dimensional radiative-equilibrium models for hot Jupiter planets generally show that the atmospheric opacity is dominated by water vapor, which is especially high in the mid-infrared, but has prominent windows (the JHK bands) in the near infrared (Fortney et al. 2008; Burrows et al. 2008). One can probe more deeply, to gas at higher pressure, in these opacity windows. Models without temperature inversions feature strong emission in the JHK bands, since one sees down to the hotter gas. Models with temperature inversions, since they feature a relatively hotter upper atmosphere and relatively cooler lower atmosphere, yield weaker emission in the near-IR (JHK), but stronger emission in the mid-infrared (Hubeny et al. 2003; Fortney et al. 2006). Near-infrared thermal emission measurements should thus be useful to determine whether TrES-2b does or does not harbour a temperature inversion.

Owing to its high irradiation, with an incident flux of $\sim 1.1 \times 10^9\ ergs^{-1}cm^{-2}$, and favourable planet-to-star radius ratio ($R_P/R_* \sim 0.13$), we included TrES-2b in our program observing the secondary eclipses of some of the hottest of the hot Jupiters from the ground. Here we present Ks-band observations bracketing TrES-2b's secondary eclipse using the Wide-field InfraRed Camera (WIRCam) on the Canada-France-Hawaii Telescope (CFHT). We report a 5σ detection of its thermal emission.

2. OBSERVATIONS AND DATA REDUCTION

We observed TrES-2 (K=9.846) with WIRCam (Puget et al. 2004) on CFHT on 2009 June 10 under photometric conditions. The observations lasted for $\sim$3.5 hours evenly bracketing the predicted secondary eclipse of this hot Jupiter assuming it has a circular orbit. Numerous reference stars were also observed in the 21x21 arcmin field of view of WIRCam. To minimize the impact of flat field errors, intrapixel variations and to keep the flux of the target star well below detector saturation, we defocused the telescope to 1.5mm, such that the flux of our target was spread over a ring $\sim$20 pixels in diameter ($6''$) on our array.

We observed TrES-2 in "stare" mode on CFHT where the target star is observed continuously without dithering. 5-second exposures were used to avoid saturation. To increase the observing efficiency we acquired a series of data-cubes each containing twelve 5-second exposures. The twelve exposure data-cube is the maximum number of exposures allowed in a guide-cube in queue mode at CFHT. To counteract drifts in the position of the stars positions on the WIRCam chips, which we had noticed in earlier WIRCam observations of secondary eclipses (Croll et al. 2010a), we initiated a corrective guiding "bump" before every image cube to recenter the stellar point-spread-function as near as possible to the original pixels at the start of the observation. The effective duty cycle after accounting for readout and for saving exposures was 43%. The images were preprocessed with the 'I'iwi pipeline[6]. This pipeline includes the following steps: applying a non-linearity flux correction, removing bad and saturated pixels, dark subtraction, flat-fielding, sky subtraction, zero-point calibration and a rough astrometry determination. We sky subtract our data by constructing a normalized sky frame built by taking the median of a stack of source-masked and background-normalized on-sky images. Our on-sky images consist of 15 dithered in-focus images observed before and after the on-target sequence. For each on-target image the normalized sky frame is scaled to the target median background level and then subtracted.

We performed aperture photometry on our target star and all unsaturated, reasonably bright reference stars on the WIRCam array. We used a circular aperture with a radius of 12.5 pixels. We tested larger and smaller apertures in increments of 0.5 pixels, and confirmed that this size of aperture returned optimal photometry. The residual background was estimated using an annulus with an inner radius of 21 pixels, and an outer radius of 30 pixels; a few different sizes of sky annuli were tested, and it was found that the accuracy of the resulting photometry was not particularly sensitive to the size of the sky aperture. As TrES-2 has a nearby reference star ($0.17'$ separation) that falls in our sky aperture, we exclude a slice of the annulus that falls near this reference star to avoid any bias in background determination[7]. During our observations, despite the aforementioned corrective "bump" to keep the centroid of our stellar point-spread-function (PSF) as steady as possible, our target star and the rest of the stars on our array displayed high frequency shifts in position (Figure 1). To ensure that the apertures for our photometry were centered in the middle of the stellar PSFs, we used a center-of-mass calculation, with pixel flux substituted for mass, to determine the x and y center of our defocused stellar rings for each one of our target and reference star apertures.

The light curves for our target and reference stars following our aperture photometry displayed significant, systematic variations in intensity (see the top panel of Figure 2), possibly due to changes in atmospheric transmission, seeing and airmass, guiding errors and/or other effects. The target light curve was then corrected for these systematic variations by normalizing its flux to the 11 reference stars that show the smallest deviation from the target star outside of the expected occultation. Reference stars that showed significant deviations in-eclipse from that of the target star and other reference stars, as indicated by a much larger root-mean-square in-eclipse than out-of-eclipse due to intermittent systematic effects for instance, were also excluded. For the reference stars that were chosen for the comparison to our target star, the flux of each one of these star was divided by its median-value, and then an average reference star light curve was produced by taking the mean of the lightcurves of these median-corrected reference stars. The target flux was then normalized by this mean reference star light curve.

Figure 3 marks the 11 reference stars used to correct the flux of our target; the 2MASS identifiers of the refer-

[6] http://www.cfht.hawaii.edu/Instruments/Imaging/WIRCam/IiwiVersion1Doc.html

[7] Pixels that fall from 5^o to -45^o degrees as measured from due North towards the East are excluded from our annulus.

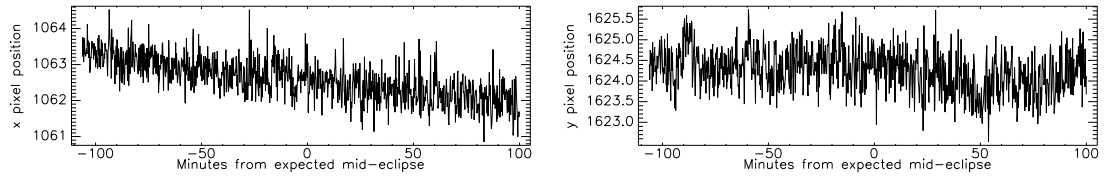

FIG. 1.— The x and y position of the centroid of the PSF of the target star, TrES-2, with time (top panels).

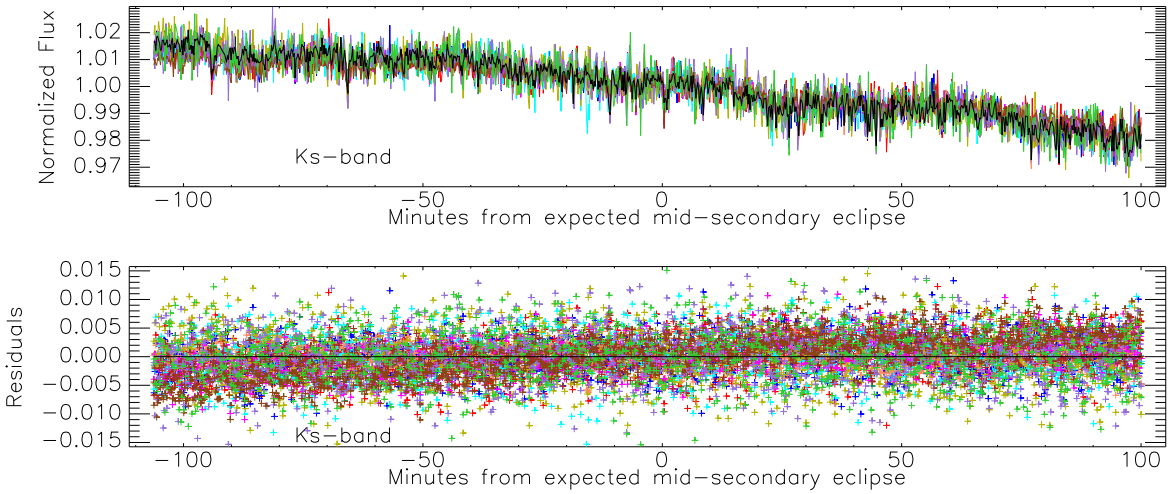

FIG. 2.— Top panel: The normalized flux from the target star (black) and the reference stars that are used to calibrate the flux of TrES-2b (various colours). Bottom panel: The residuals from the normalized flux of the target star of the normalized flux of the reference stars (various colours). The residuals have not been corrected for the x/y pixel positions of the target.

TABLE 1
REFERENCE STARS

Reference Star #	2MASS Identifier	K-band Magnitude
1	J19072977+4918354	10.294
2	J19065501+4916195	10.737
3	J19071365+4912041	11.270
4	J19065809+4916315	9.875
5	J19070093+4917323	11.337
6	J19074435+4915418	10.766
7	J19071824+4916526	11.239
8	J19073380+4916035	10.712
9	J19071955+4911176	11.514
10	J19075629+4923281	9.671
11	J19065548+4925404	11.454

ence stars are given in Table 1. Note that the majority of the reference stars with the smallest out of occultation residuals to our target star are on the same chip as our target, despite the fact that there are other reference stars on other chips closer in magnitude to our target. We believe this is due to the differential electronic response of the different WIRCam chips, and have noticed this same effect with other WIRCam observations of other hot Jupiter secondary eclipses (Croll et al. 2010a).

Following this correction we noticed that the flux of our target and reference stars displayed near-linear correlations with the x or y position of the centroid of the stellar PSF on the chip. Given the aforementioned high frequecy of these shifts (Fig. 1) this suggests that any leftover trend with position and the flux of the star was

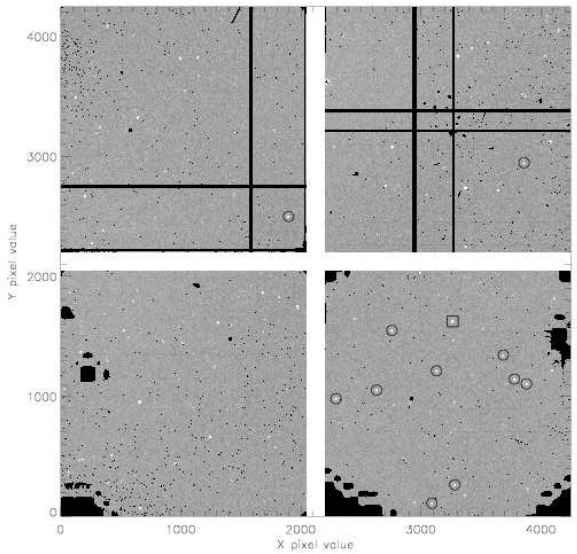

FIG. 3.— The CFHT/WIRCam full frame array during our observations of TrES-2b. The image has been preprocessed with the 'I'iwi pipeline; the obvious artifacts (in the lower-left corners of the bottom two chips for instance or the crosses on the upper two chips) are due to the masking of bad pixels. The target star, TrES-2 (large square on the lower-right chip), and the reference stars used to correct the flux of TrES-2 (circles) are marked.

instrumental in origin. Thus these near-linear trends (Figure 4 top panels) were removed from the data for both the target and reference stars by performing a fit to the x and y position of the centroid of the PSF and the normalized flux for the out-of-eclipse photometry. We fit

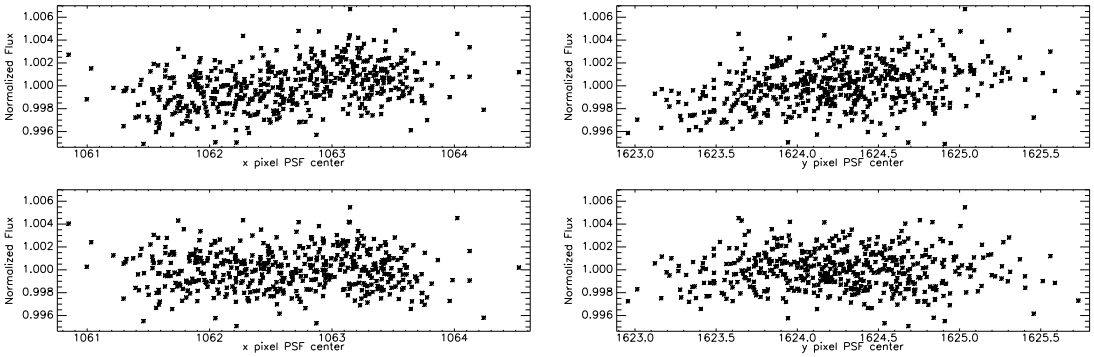

FIG. 4.— The out-of-eclipse photometry prior to the correction for the x and y position of the PSF (top panels). The out-of-eclipse photometry following this correction (bottom panels; see §2 for details).

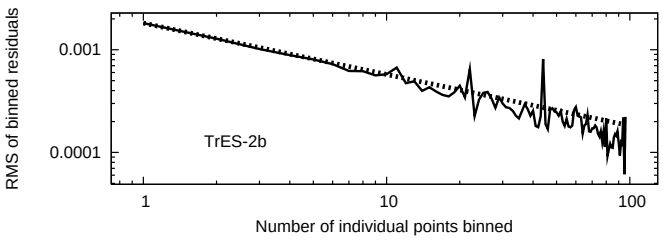

FIG. 5.— The root-mean-square of our out-of-eclipse photometry (solid line) following the various corrections documented in §2. The dashed line displays the one over the square-root of the bin-size expectation for gaussian noise.

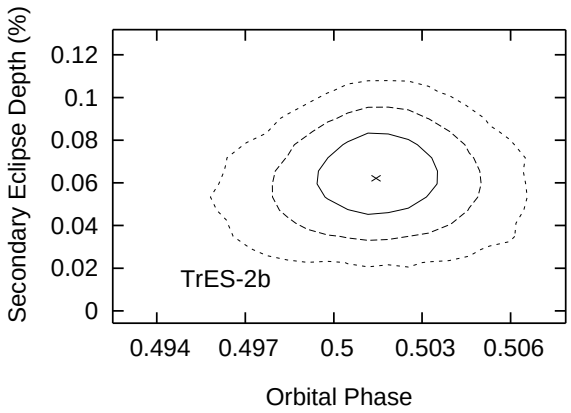

FIG. 6.— The 68.3% (1σ; solid-line), 95.5% (2σ; dashed-line) and 99.7% (3σ; short dashed-line) credible regions from our MCMC analysis on the secondary eclipse depth, ΔF, and phase, ϕ. The "x" in the middle of the plot denotes the best-fit point from our MCMC analysis.

the out-of-eclipse photometric flux to the x and y position of the centroid of the PSF with a function of the following form:

$$f = 1 + d_1 x + d_2 y + d_3 xy \quad (1)$$

where d_1, d_2, and d_3 are constants. We then apply this correction to both the in-eclipse and out-of-eclipse photometry. The out-of-eclipse photometric data prior to and following this correction are displayed in Figure 4 (bottom panels). No other trends that were correlated with instrumental parameters were found.

By correcting the flux of our target with these 11 reference stars and by removing the above correlation with the x/y position on the chip the point-to-point scatter of our data outside occultation improves from a root-mean-square (RMS) of 13.7×10^{-3} to 0.71×10^{-3} per every 58 s (or 5 images). The photometry following the aforementioned analysis is largely free of systematics, as evidenced by the fact that the out-of-eclipse photometric precision lies near the gaussian noise expectation for binning the data of one over the square-root of the bin-size (Figure 5). Our observations in Ks-band, though, are still well above the predicted photon noise RMS limit of 2.3×10^{-4} per 58 seconds. For the following analysis we set the uncertainty on our individual measurements as 0.95 times the RMS of the out of eclipse photometry after the removal of a linear-trend with time; we found simply using 1.0 times the RMS of the out-of-eclipse photometry resulted in a reduced χ^2 below one, and thus resulted in a slight over-estimate of our errors.

3. ANALYSIS

Similarly to nearly all our near-infrared photometric data-sets taken with CFHT/WIRCam (e.g. Croll et al. 2010a,b), our Ks-band photometry following the reduction exhibited an obvious background trend, B_f. This background term displayed a near-linear slope, and thus we fit the background with a linear-function of the form:

$$B_f = 1 + c_1 + c_2 dt \quad (2)$$

where dt is the time interval from the beginning of the observations, and c_1 and c_2 are the fit parameters. Given that most of our other data-sets display these background trends, it is unlikely, but not impossible, that this slope is intrinsic to TrES-2. We fit for the best-fit secondary eclipse and linear fit simultaneously using Markov Chain Monte Carlo (MCMC) methods (Christensen et al. 2001; Ford 2005; described for our purposes in Croll 2006). We use a 5×10^6 step MCMC chain. We fit for c_1, c_2, the depth of the secondary eclipse, ΔF, and the offset that the eclipse occurs later than the expected eclipse center, $t_{\rm offset}$[8]. We also quote the best-fit phase, ϕ, as well as the best-fit mid-eclipse heliocentric julian-date, $t_{eclipse}$. We use the Mandel & Agol (2002) algorithm without limb darkening to generate our best-fit secondary eclipse model. We obtain our stellar and planetary parameters for TrES-2 from Torres et al. (2008), including the planetary period and ephemeris. The results from these fits are presented in Table 2. The phase dependence of the best-fit

[8] we take into account the 0.6 minute offset due to light travel-time in the system [Loeb 2005]

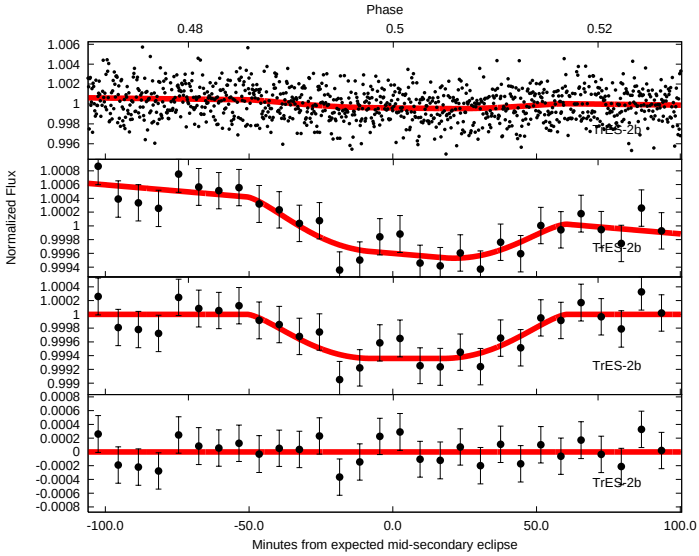

FIG. 7.— CFHT/WIRCam Ks-band photometry of the secondary eclipse of TrES-2b. The top panel shows the unbinned lightcurve, while the panel that is the second from the top shows the lightcurve with the data binned every 7.0 minutes. The panel that is the second from the bottom shows the binned data after the subtraction of the best-fit background, B_f, while the bottom panel shows the binned residuals from the best-fit model. In each one of the panels the best-fit best-fit secondary eclipse and background, B_f, is shown with the red line. The expected mid-secondary eclipse is if TrES-2b has zero eccentricity.

TABLE 2
BEST-FIT SECONDARY ECLIPSE PARAMETERS

Parameter	MCMC Solution	"Residual permutation" Solution
reduced χ^2	$1.089^{+0.003}_{-0.002}$	$1.086^{+0.018}_{-0.001}$
ΔF	$0.062^{+0.013}_{-0.011}$%	$0.064^{+0.005}_{-0.005}$%
t_{offset} (min)[a]	$4.5^{+4.8}_{-4.6}$	$3.8^{+4.6}_{-3.0}$
$t_{eclipse}$ (HJD-2440000)	$14994.0605^{+0.0033}_{-0.0032}$	$14994.0600^{+0.0032}_{-0.0021}$
c_1	$0.00061^{+0.00010}_{-0.00012}$	$0.00061^{+0.00008}_{-0.00007}$
c_2 (d^{-1})	$-0.005^{+0.001}_{-0.001}$	$-0.005^{+0.001}_{-0.002}$
ϕ [a]	$0.5014^{+0.0013}_{-0.0013}$	$0.5012^{+0.0013}_{-0.0008}$
T_B (K)	1636^{+79}_{-88}	1646^{+29}_{-30}
$e\cos(\omega)$ [a]	$0.0020^{+0.0021}_{-0.0021}$	$0.0017^{+0.0020}_{-0.0020}$
f_{Ks}	$0.358^{+0.074}_{-0.072}$	$0.367^{+0.027}_{-0.026}$

[a] We account for the increased light travel-time in the system (Loeb 2005).

secondary eclipse is presented in Figure 6. The best-fit secondary eclipse is presented in Figure 7.

To determine the effect of any excess systematic noise on our photometry and the resulting fits we employ the "residual-permutation" method as discussed in Winn et al. (2009). In this method the best-fit model is subtracted from the data, the residuals are shifted between 1 and the total number of data points (N=1056 in our case), and then the best-fit model is added back to the residuals. We then refit the adjusted lightcurve with a 5000-step MCMC chain and record the parameters of the lowest χ^2 point reached. By inverting the residuals we are able to perform $2N-1$ total iterations. The best-fit parameters and uncertainties obtained with this method are similar to those found for our MCMC method and are listed in Table 2. As the two methods produce similar results we employ the MCMC errors for the rest of this paper. We also test for autocorrelation among the residuals to our best-fit model using the Durbin-Watson test (Durbin & Watson 1951); for the Durbin-Watson test a test-statistic greater than 1.0 and less than 3.0 (ideally near 2.0) indiciates a lack of autocorrelation. Our residuals pass this test with a test-statistic of 1.97.

4. DISCUSSION

The depth of our best-fit secondary eclipse is $0.062^{+0.013}_{-0.011}$%. The reduced χ^2 is 1.089. Our best-fit secondary eclipse is consistent with a circular orbit; the offset from the expected eclipse center is: $t_{offset} = 4.5^{+4.8}_{-4.6}$ minutes (or at a phase of ϕ=$0.5014^{+0.0013}_{-0.0013}$). This corresponds to a limit on the eccentricity and argument of periastron of $e\cos\omega = 0.0020^{+0.0021}_{-0.0021}$, or a 3σ limit of $|e\cos\omega| < 0.0090$). Our result is fully consistent with the more sensitive $e\cos\omega$ limits reported from the secondary eclipse detections at the four Spitzer/IRAC wavelengths (O'Donovan et al. 2009). Thus our result bolsters the conclusion of O'Donovan et al. (2009) that tidal damping of the orbital eccentricity is unlikely to be responsible for "puffing up" the radius of this exoplanet.

A secondary eclipse depth of $0.062^{+0.013}_{-0.011}$% corresponds to a brightness temperature of $T_B = 1636^{+79}_{-88}$ K in the Ks-band assuming the planet radiates as a blackbody, and adopting a stellar effective temperature of $T_{eff} = 5850 \pm 50$ (Sozzetti et al. 2007). This compares to the equilibrium temperature of TrES-2b of T_{eq}~1472 K assuming isotropic reradiation, and a zero Bond albedo. Hot Jupiter thermal emission measurements allow joint constraints on the Bond albedo, A_B, and the efficiency of day to nightside redistribution of heat on these presumably tidally locked planets. The Bond albedo, A_B is the fraction of the bolometric, incident stellar irradiation that is reflected by the planet's atmosphere. We parameterize the redistribution of dayside stellar radiation absorbed by the planet's atmosphere to the nightside by the reradiation factor, f, following the Lopez-Morales & Seager (2007) definition. If we assume a Bond albedo near zero, consistent with observations of other hot Jupiters (Charbonneau et al. 1999; Rowe et al. 2008) and with model predictions (Burrows et al. 2008b), we find a reradiation factor of $f_{Ks} = 0.358^{+0.074}_{-0.072}$ from our Ks-band eclipse photometry only, indicative of relatively efficient advection of heat from the day-to-nightside at this wavelength. In comparison, the reradiation factor for an atmosphere that reradiates isotropically is f=$\frac{1}{4}$, while f=$\frac{1}{2}$ denotes redistribution and reradiation over the dayside face only.

Our secondary eclipse depth, when combined with the secondary eclipse depths at the Spitzer/IRAC wavelengths from O'Donovan et al. (2009), is consistent with a range of Bond albedos, A_B, and efficiencies of the day to nightside redistribution on this presumably tidally locked planet (Figure 8). The best-fit total reradiation factor, f_{tot}, that results from a χ^2 analysis of all the eclipse depths for TrES-2b assuming a zero Bond albedo

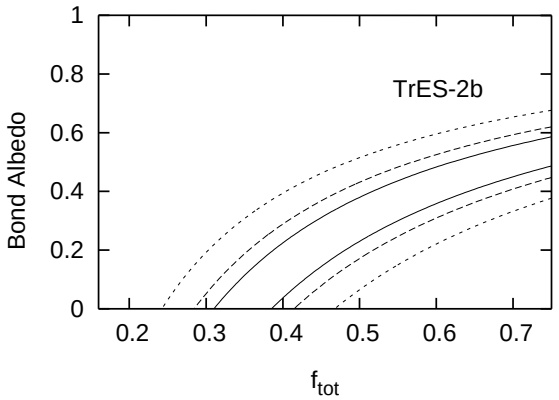

FIG. 8.— The 68.3% (1σ; solid-line), 95.5% (2σ; dashed-line) and 99.7% (3σ; short dashed-line) χ^2 confidence regions on the reradiation factor, f_{tot}, and Bond albedo from the combination of our Ks-band point and the Spitzer/IRAC measurements (O'Donovan et al. 2009).

is $f_{tot} = 0.346^{+0.038}_{-0.037}$. Thus our Ks-band brightness temperature ($T_B = 1636^{+79}_{-88}$ K) and reradiation factor f_{Ks}=$0.358^{+0.074}_{-0.072}$, reveal an atmospheric layer that is similar to, and perhaps slightly hotter, than the atmospheric layers probed by longer wavelength Spitzer observations (T_B~1500 K from Spitzer/IRAC observations of TrES-2b [O'Donovan et al. 2009]). The Ks-band is expected to be at a minimum in the water opacity (Fortney et al. 2008; Burrows et al. 2008), and thus our Ks-band observations are expected to be able to see deep into the atmosphere of TrES-2b. Our observations suggest that the deep, high pressure atmosphere of TrES-2b displays a similar temperature – perhaps a slightly warmer temperature – to lower pressure regions.

Another way of parameterizing the level of day-to-nightside heat redistribution is calculating the percentage of the bolometric luminosity emitted by the planet's dayside, L_{day}, compared to the nightside emission, L_{night}. Measurements of the thermal emission of a hot Jupiter at its blackbody peak provide a valuable constraint on the bolometric luminosity of the planet's dayside emission, and by inference its nightside emission (Barman 2008). From simple thermal equilibrium arguments if TrES-2b has a zero Bond albedo and it is in thermal equilibrium with its surroundings it should have a total bolometric luminosity of $L_{tot} = 7.7\times10^{-5}L_{\odot}$. By integrating the luminosity per unit frequency of our best-fit blackbody model across a wide wavelength range we are able to calculate the percentage of the total luminosity reradiated by the dayside as ~69% ($L_{day} = 5.3\times10^{-5}L_{\odot}$). The remainder, presumably, is advected via winds to the nightside.

We compare the depth of our Ks-band eclipse and the Spitzer/IRAC eclipses (O'Donovan et al. 2009) to a series of planetary atmosphere models in Figure 9. This comparison is made quantitatively as well as qualitatively by integrating the models over the WIRCam Ks band-pass as well as the Spitzer/IRAC channels, and calculating the χ^2 of the thermal emission data compared to the models. We first plot blackbody models with an isotropic reradiation factor (f=$\frac{1}{4}$; blue dotted-line) and that of our best-fit value (f=0.346; grey dotted-line) these models have dayside temperatures of T_{day}~1496K

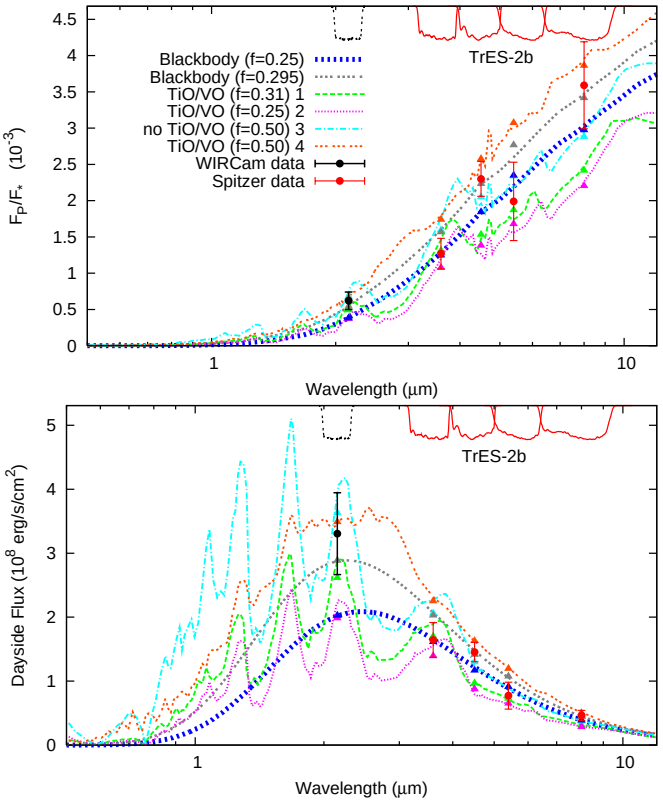

FIG. 9.— Dayside planet-to-star flux ratios (top) and dayside flux at the planet's surface (bottom). The Ks-band point (black point; ~2.15 μm) is our own, while the Spitzer/IRAC red points are from O'Donovan et al. (2009). Blackbody curves for isotropic reradiation (f=$\frac{1}{4}$; T_{eq}~1496 K; blue dashed-line) and for our best-fit reradiation factor (f=0.346; T_{eq}~1622 K; grey dotted-line) are also plotted. We also plot one-dimensional, radiative transfer spectral models (Fortney et al. 2006, 2008) for various reradiation factors and with and without TiO/VO. The models with TiO/VO include f=$\frac{1}{4}$ (purple dotted line), f=0.31 (green dashed line), and f =$\frac{1}{2}$ (orange dotted line); only the last of the models has a temperature inversion. The model without TiO/VO features emission from the dayside only (f=$\frac{1}{2}$; cyan dot-dashed line). The models on the top panel are divided by a stellar atmosphere model (Hauschildt et al. 1999) of TrES-2 using the parameters from Torres et al. (2008) (M_*=0.98 $M_{\odot}$, R_*=1.00 $R_{\odot}$, T_{eff}=5850 K, and log g= 4.43). We plot the Ks-band WIRCam transmission curve (dotted black lines) and Spitzer/IRAC curves (solid red lines) inverted at arbitrary scale at the top of both panels.

and T_{day}~1622K, respectively. Both blackbody models provide reasonable fits to the data, although the latter model (f=0.346; χ^2=4.7) provides a definitively better fit than the former isothermal model (f=$\frac{1}{4}$; χ^2=9.1) as it better predicts our Ks-band emission and the Spitzer/IRAC 8.0 μm emission. This suggests that overall TrES-2b has a near-isothermal dayside temperature-pressure profile and is well-fit by a blackbody.

We thus also compare the data to a number of one-dimensional, radiative transfer, spectral models (Fortney et al. 2006, 2008) with different reradiation factors that specifically include or exclude gaseous TiO and VO into the chemical equilibrium and opacity calculations. In these models when TiO and VO are present they act as absorbers at high altitude and lead to a hot stratosphere and a temperature inversion (Hubeny et al. 2003). However, if the temperature becomes too cool (TiO and VO start to condense at 1670

K at 1 mbar [Fortney et al. 2008]), TiO and VO condense out and the models with and without TiO/VO are very similar. In the case of TrES-2b, for all the models we calculate, except our model that features dayside emission only (f=$\frac{1}{2}$), they do not harbour temperature inversions because the atmospheres are slightly too cool and TiO/VO has condensed out of their stratospheres. We plot models with TiO/VO and reradiation factors of f=$\frac{1}{4}$ (purple dotted line), f=0.31 (green dashed line), and f=$\frac{1}{2}$ (orange dotted line), and without TiO/VO with a reradiation factor of f=$\frac{1}{2}$ (cyan dot-dashed line). O'Donovan et al. (2009) argued that TrES-2b experienced a temperature inversion due to the high 4.5 μm emission compared to the low 3.6 μm emission, which was predicted to be a sign of water and CO in emission, rather than absorption, in TrES-2b's presumably inverted atmosphere. We also find that our models without a temperature inversion have difficultly matching the Spitzer/IRAC 5.6 and 8.0 μm thermal emission (χ^2=25.4 for f=$\frac{1}{4}$ with TiO/VO, χ^2=15.3 for f=0.31 with TiO/VO, and χ^2=5.5 for f=$\frac{1}{2}$ without TiO/VO). If the temperature inversion is due to TiO/VO, by the time the atmosphere becomes hot enough that TiO/VO remains in gaseous form, the thermal emission is too bright to fit the 3.6, and 5.8 μm thermal emission (χ^2=10.6 for f=$\frac{1}{2}$ with TiO/VO).

The combination of our blackbody and radiative transfer models with our own eclipse depth and those from the Spitzer/IRAC instrument (O'Donovan et al. 2009) thus suggest that the atmosphere of TrES-2b likely features modest redistribution of heat from the day to the nightside. It is unclear whether the atmosphere of TrES-2b requires a temperature inversion. A simple blackbody model (f=0.346 and T_{eq}∼1622 K) provides an exemplary fit to the data; this may indicate that TrES-2b has a fairly isothermal dayside temperature structure, perhaps similar to HAT-P-1b (Todorov et al. 2010). An important caveat, on the above result is that our f=$\frac{1}{2}$ model without TiO/VO (χ^2=5.5) and thus without a temperature inversion returns nearly as good of fit as our best-fit blackbody model (f=0.346; χ^2=4.7); thermal emission measurements at other wavelengths, and repeated measurements at the above wavelengths, are thus necessary to differentiate a blackbody-like spectrum, from significant departures from blackbody-like behaviour, and to confirm that TrES-2b efficiently redistributes heat to the nightside of the planet. Specifically, the variations between the models displayed in Figure 9 are largest in the near-infrared J & H-bands and thus further near-infrared constraints – if they are able to achieve sufficient accuracy to measure the small thermal emission signal of TrES-2b in the near-infrared – should prove eminently useful to constrain the atmospheric characteristics of this planet.

If the excess emission at 4.5 μm is due to water emission, rather than absorption, due to a temperature inversion in the atmosphere of TrES-2b then the inversion is unlikely to be due to TiO/VO. This is because the atmosphere of TrES-2b appears too cool to allow TiO/VO to remain in gaseous form in its upper atmosphere. If there is a temperature inversion then the high altitude optical absorber is likely to be due to another chemical species than TiO/VO. For instance, Zahnle et al. (2009) have investigated the photochemistry of sulphur-bearing species as another alternative.

TrES-2b is a promising target for the characterization of its thermal emission across a wide wavelength range. In addition to orbiting a relatively bright star, and having a favourable planet-to-star radius ratio, TrES-2 lies within the Kepler field. The combination of secondary eclipse measurements already published using Spitzer/IRAC, upcoming measurements with Kepler (∼430 - 900 nm; Borucki et al. 2008), and J, H and K-band near-infrared measurements that could be obtained from the ground, will allow us to fully constrain TrES-2b's energy budget. At the shorter end of this wavelength range it should also be possible to constrain the combination of reflected light and thermal emission. Our results predict that even if the geometric albedo of TrES-2b is as low as 5% in the Kepler bandpass, if Kepler is able to detect the secondary eclipse of this planet then it will be detecting a significant fraction of reflected light in addition to thermal emission. This will largely break the degeneracy on the Bond albedo and the reradiation factor for this planet, facilitating a more complete understanding of its energy budget.

The Natural Sciences and Engineering Research Council of Canada supports the research of B.C. and R.J. The authors would like to thank Marten van Kerkwijk for helping to optimize these observations, and Norman Murray for useful discussions. The authors especially appreciate the hard-work and diligence of the CFHT staff in helping us pioneer this "stare" method on WIRCam. We thank the anonymous referee for a thorough review.

REFERENCES

Barman, T.S. 2008, ApJ, 676, L61
Borucki, W. et al. 2008, Transiting Planets, Proceedings IAU Symposium No. IAUS253, 289
Burrows, A. et al. 2008, ApJ, 678, 1436
Burrows, A. et al. 2008b, ApJ, 682, 1277
Charbonneau, D. et al. 1999, ApJ, 522, L145
Charbonneau, D. et al. 2000, ApJ, 529, L45
Charbonneau, D. et al. 2005, ApJ, 626, 523
Christensen, N. et al. 2001, Classical Quantum Gravity, 18, 2677
Croll, B. 2006, PASP, 118, 1351
Croll, B. et al. 2010a, ApJ, submitted 2010 January 31
Croll, B. et al. 2010b, AJ, submitted 2010 April 29
de Mooij, E.J.W. & Snellen, I.A.G. 2009, A&A, 493, L35
Deming, D. et al. 2005, Nature, 434, 740
Durbin, J. & Watson, G.S. 1951, Biometrika, 38, 159
Fazio, G.G. et al. 2004, ApJS, 154, 10
Ford, E.B. 2005, AJ, 129, 1706
Fortney, J.J, et al. 2006, ApJ, 642, 495
Fortney, J.J, et al. 2008, ApJ, 678, 1419
Gillon, M. et al. 2009, A&A, astro-ph/0905.4571
Hauschildt, P.H. et al. 1999, ApJ, 512, 377
Henry, G.W. et al. 2000, ApJ, 529, L41
Hubeny, I. et al. et al. 2003, ApJ, 594, 1011
Loeb, A. 2005, ApJ, 623, L45
Lopez-Morales, M. & Seager, S. 2007, ApJ, 667, L191
Mandel, K. & Agol, E. 2002, ApJ, 580, L171
O'Donovan, F.T. et al. 2006, ApJ, 651, L61
O'Donovan, F.T. et al. 2009, ApJ, submitted, astro-ph/0909.3073
Puget, P. et al. 2004, SPIE, 5492, 978
Rowe, J. F et al. 2008, ApJ, 689, 1345

Sing, D.K. & Lopez-Morales, M. 2009, A&A, 493, L31
Sozzetti, A. et al. 2007, ApJ, 664, 1190
Swain, M.R. et al. 2009, ApJ, 690, L114
Todorov, K. et al. 2010, ApJ, 708, 498
Torres, G. et al. 2008, ApJ, 677, 1324
Winn, J. N et al. 2009, ApJ, 693, 794
Zahnle, K. et al. 2009, ApJ, 701, 20